AIAA JOURNAL
Vol. 33, No. 8, August 1995

Self-Sustained Flow Oscillation in a Ducted Combustor with Multiple Inlets

Tong-Miin Liou* and Yi-Yung Wu†
National Tsing Hua University, Hsinchu 30043, Taiwan, Republic of China

The impingement flowfield in a ducted combustor with one axial inlet and dual side inlets was characterized qualitatively by smoke flow visualization as well as quantitatively by laser Doppler velocimetry and microphone measured velocity and wall pressure spectral characteristics, respectively. The baseline momentum ratio *MR* of the axial inlet to side inlets was chosen to be 0.27. In this case, a resonant feedback frequency of 365 Hz, which prevailed in the entire combustor, and the second and the third harmonics, which appeared near the impingement region, were observed. The effect of *MR* on the flow oscillations was further studied, and the results showed that a constant Strouhal number, based on the axial inlet velocity and width, of 0.013 was found for $MR \leq 0.94$, and Reynolds number of 10^3–10^4 and the frequency of the oscillations varied linearly with the *MR*. From the investigation of the measured spectra, the feedback mechanism with appropriately proposed feedback distance and convective velocity, and of the chamber resonance curve, the onset of the oscillations was interpreted to be triggered by the coupling between the disturbance feedback frequency and the acoustic frequency of the chamber.

Nomenclature

a_0 = speed of sound
f_d = distinct peak frequency, Hz
f'_f = predicted feedback frequency, Hz
f_f = feedback frequency, Hz
H = combustor height, 30 mm
L = feedback distance
L_d = dome height, 15 mm
L_r = reattachment length
MR = momentum ratio of the axial inlet to side inlets
Re_c = combustor Reynolds number, $\equiv HU_r/\nu$
Re = axial inlet Reynolds number, $\equiv W_f U_a/\nu$
S = Strouhal number, $\equiv f W_f/U_a$
U = longitudinal mean velocity
U_a = bulk mean velocity of the axial inlet
U_c = convective speed of the coherent shedding vortices
U_j = jet exit velocity
U_r = combustor bulk mean velocity
U_s = bulk mean velocity of the side inlets
V = transverse mean velocity
W_a = width of the side inlet, 15 mm
W_f = width of the axial inlet, 1.6 mm
X = combustor axial coordinate
X^* = normalized combustor axial coordinate, $\equiv X/H$
Y = combustor transverse coordinate
Y^* = normalized combustor transverse coordinate, $\equiv Y/(H/2)$
Z = combustor spanwise coordinate
Z_c = combustor spanwise width, 120 mm
Z^* = normalized combustor spanwise coordinate, $\equiv Z/(Z_c/2)$

Introduction

SELF-SUSTAINED oscillations of impingement flows occur frequently in a wide variety of inner or outer flow configurations; they provoke noises, structural loading, and combustion instabilities.[1–5] In the present work, the flow oscillations in a ducted flow with multiple impinging flows are investigated by means of flow visualization and spectral analyses of the velocity components and the wall pressure.

From a practical point of view, the impingement of multiple flows on each other is a crucial feature of the flowfield inside a combustor. As multiple streams of fuel and air are introduced into the combustor, the fluid mixing and the combustion process occur primarily in the impingement region of the fuel and airstreams. To achieve a high-combustion efficiency, good mixing and a stable flowfield in the combustor are required. Studies on the flow characteristics and fluid mixing in combustors have been reported by several researchers.[6–9] Aside from the fluid mixing problem, the phenomenon of oscillations in the combustors has been of concern because the presence of large oscillations results in a serious reduction in the combustion performance. Therefore, an understanding of the oscillation mechanism in the combustor is of practical importance.

The combustion-induced pressure oscillations in a side dump ramjet combustor with two side inlets were studied by Clark.[4] He found a predominant frequency of around 300 Hz, which was related to the longitudinal acoustic modes, and also pointed out the connection between the unsteady heat release and fluid dynamics. Dunlap and Brown[3] illustrated that the interaction between the vortex shedding and acoustics in a segmented solid propellant rocket motor chamber and demonstrated that the coupling between the flow and acoustics resulted in a significant increase in the pressure amplitude. Byrne[5] studied the longitudinal pressure oscillations in coaxial- and side-dump combustors and concluded that the large-amplitude oscillations result from the close match between the resonant feedback frequency and the natural acoustic frequency, for instance, the longitudinal mode frequency and the Helmholtz frequency, of the combustor. On the other hand, the impingement of flows lead to flow-induced velocity and pressure oscillations and was one probable mechanism responsible for initiating combustion instabilities. Schadow et al.[10] investigated the acoustically forced flow in a coaxial dump duct using a hot-wire anemometer and found that highly coherent, large-scale structures were generated under the proper forcing conditions. The preceding brief survey suggests that an understanding of the impingement of multiple jets in ducted flow is an important topic in enhancing fluid mixing and avoiding combustion instabilities.

From the survey it is also noted that the spectral study of flow oscillations in the combustor with three inlets is still lacking. Consequently, in the present paper the oscillations in a combustor with dual side inlets and one axial inlet are investigated by visualizing the flow patterns and analyzing the velocity and wall pressure spectral characteristics. A case of momentum ratio MR of the axial inlet to the side inlets was chosen as the baseline case to illustrate the variation of the spectra at different locations in the combustor. Then, the relationship between the oscillation frequency and MR is presented. Finally, an explanation of the mechanism triggering the dominant peak frequency is also provided.

Received March 13, 1993; revision received June 13, 1994; accepted for publication Oct. 5, 1994.

*Professor, Department of Power Mechanical Engineering.
†Graduate Student, Department of Power Mechanical Engineering.

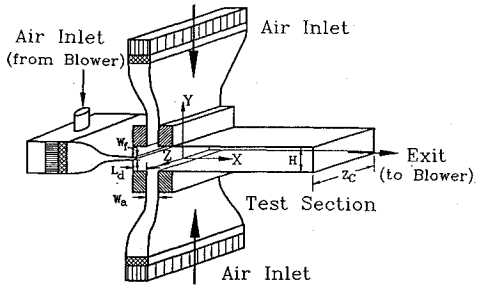

Fig. 1 Configuration and coordinate system of the model.

Experimental Facility and Conditions

Test Model

The model was made of Plexiglas® and the dimensions are listed in the Nomenclature. One axial inlet was located at the center of the dome plate ($X^* = -1.0$), and two side inlets were intersected perpendicularly on the upper and the lower duct wall, as shown in Fig. 1. Side-inlet flows were drawn into the test chamber through the settling chambers, honeycombs, screens, and 10:1 contractions by a 10-hp dc motor driven turbo blower located at the downstream end. In between the test duct and the blower there was a well-designed noise reduction chamber with a dimension of $100 \times 130 \times 80$ cm^3 to reduce the passage and mechanical vibration noises generated from the blower. The axial flow was blown into the test chamber through the honeycombs, screens, and a 152:1 contraction by another 5-hp blower.

Flow Visualization Technique

Particles generated from saline solution by atomizers were used as tracers for visualizing the flow patterns in the present model. The observed area was illuminated by an argon-ion laser light sheet. The visualization results were recorded on a video tape and the pictures were enhanced by image-processing techniques to attain more visible images.

Laser Doppler Velocimetry System and Velocity Signal Processing

A two-color four-beam two-component laser Doppler velocimetry (LDV) system was set up in a backscatter configuration for the velocity measurements and described in detail in the work of Liou and Wu[9] and Liou et al.[11] The green (515.4 nm) and blue (488 nm) lines emitted from a 5-W argon-ion laser were separated into four beams and focused into the test chamber. The approximate probe volume dimensions, based on $1/e^2$ extent of light intensity, were 0.06×0.65 mm. The salt particles with a nominal diameter of 0.8 μm were introduced into the airstreams by 12 atomizers symmetrically located on the walls of the three settling chambers. The uncertainty associated with the velocity measurements and the velocity bias correction were reported in the authors' previous work.[9]

Because of the nature of the random arrival of seeding particles at the measurement volume, the power spectrum and the correlation of the LDV signals cannot be obtained directly using the conventional fast Fourier transform (FFT) algorithm, which is valid for signals with constant time intervals. Processing using an analog output signal is perhaps the most widely used method and is expected to perform well at all turbulence levels under high particle rates.[12] In the present work, therefore, a sample-and-hold digital to analog (D/A) converter circuit was employed, and the converted analog output was resampled and processed by use of an FFT analyzer to obtain the spectra. In this approach the high arrival rate of Doppler burst signals (or particle rate) is a crucial condition for acquiring bias-free spectral estimates. In order to avoid the step noise arising in the low arrival rate case,[13] the required particle rate should not be less than the reciprocal of the integral time scale. In the present experiment the integral time scale is about 10^{-3} s. After examination of the measured spectra at various particle rates, it was found that the levels of spectral peaks approached invariant as the particle rate was higher than 5,000 numbers/s. Therefore, the adequate particle rates were controlled at about from 10,000 to 20,000 numbers/s during the measurements, and the analog output of the Doppler processors was resampled at a rate of 8 kHz with a sample size of 16,000 data by the FFT analyzer. This gives a detectable frequency range of 0.5 Hz–4 kHz.

Pressure Spectrum Measurements

The wall pressure was measured using a Kulite microphone (MIC-190-140) with 1.8-mm active diameter and 100 kHz mechanical resonate frequency. The microphone was attached to pressure taps 0.3 mm in internal diameter, and the signal obtained was amplified and properly filtered by a signal conditioner (CDV-230C, Kyowa). A dual-channel FFT analyzer was used to obtain the power spectra of the wall pressure. At a given position an ensemble average typically 256 spectra was made to reduce variations of the estimated spectra.

Acoustic Resonance Measurements

To understand the acoustic resonant property of the chamber tested, a loudspeaker mounted on the dome plate ($X^* = -0.5$) and the aforementioned microphone attached to the pressure tap on the upper wall at $X^* = 1.5$ were employed to acquire the system acoustic response curve under the no-flow condition. The loudspeaker was driven by the amplified sine wave signals generated from a function generator and monitored on an oscilloscope. The signals detected by the microphone were amplified and filtered by the conditioners, analyzed by the FFT analyzer, and then fed to a personal computer for storage and further analysis.

Flow Conditions

In the present study, the MR was varied from 0.0094 to 1.28. The Reynolds number, based on the chamber height (30 mm) and the bulk mean velocity (23.9 m/s), was fixed at 4.56×10^4. The mean flow became unidirectional after $X^* = 4.0$ and reached fully developed at $X^* > 9.0$ (Ref. 9). There were two pairs of vortices formed in the flow: one located in the dome region ($-1 < X^* < 0$) and the other immediately downstream of the side-inlet ports. More detailed flow conditions and patterns are described in Ref. 9.

Results and Discussion

Visualization of the Flow Pattern

The flow patterns obtained from smoke visualization for $MR = 0.067$, 0.27, and 1.28 are shown in Fig. 2. At $MR = 0.067$, the velocity of the axial jet is so low that it is deflected back into dome region after impinging with the two side-inlet jets as shown in Fig. 2a. With increasing MR, Fig. 2b, the axial jet velocity increases. The central part of the axial jet penetrates through the crossflows formed

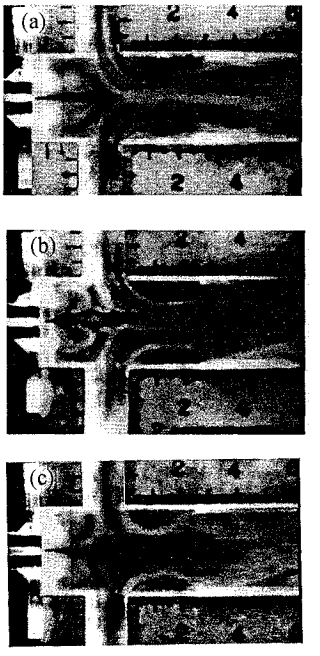

Fig. 2 Flow patterns of smoke visualization for MR: a) = 0.067, b) = 0.27, and c) = 1.28.

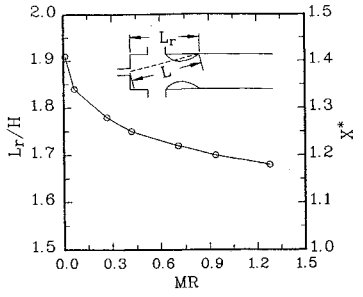

Fig. 3 Reattachment length (feedback distance) for various values of *MR*.

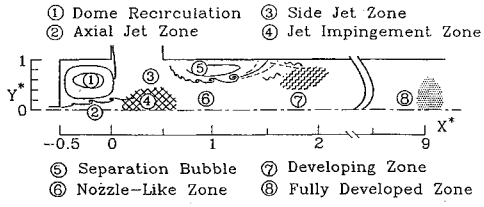

Fig. 4 Characteristic zones for the flowfield in the present model.

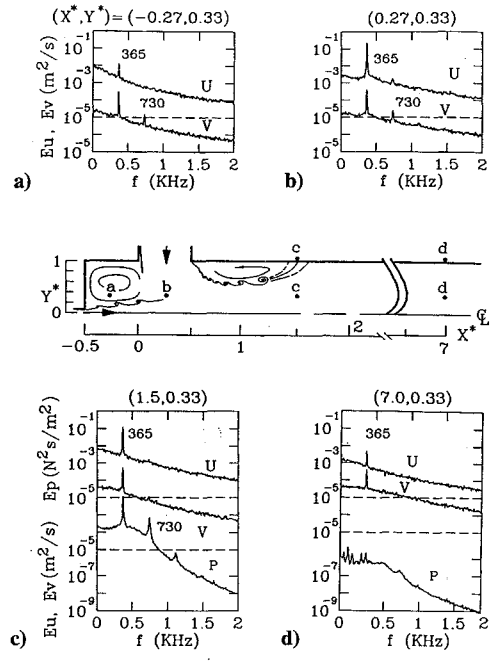

Fig. 5 Spectral density functions of the axial and transverse velocity and wall pressure fluctuations at various locations for *MR* = 0.27.

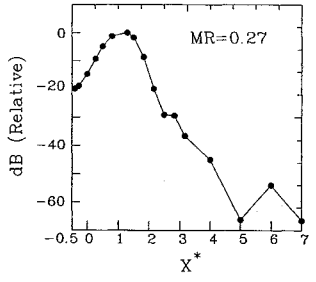

Fig. 6 Streamwise variation of energy level of fundamental frequency of fluctuating pressure for *MR* = 0.27.

by the dual side-inlet jets and proceeds downstream, whereas the edge part is deflected into the dome region. As MR increases to 1.28, it can been seen from Fig. 2c that the axial jet totally penetrates through the side jets. Notice that the vortex pattern in the dome region changes with increasing MR. For $MR = 0.067$, the dome vortex pair is mainly formed by the deflected fluids of the axial jet. When MR increases to 0.27, the counter-rotating dome vortex pairs result from the deflected edge parts of both the axial jet and the side jets. For $MR = 1.28$, as shown in Fig. 2c, the entire axial jet acts like a solid plate upon which the side jets impinge. Part of the side jet is then deflected upstream to form the dome vortex pair which rotates in the opposite direction to that shown in Fig. 2a. Also note that the reattachment length of the separation bubbles located immediately downstream of the side-inlet ports decreases with increasing MR. In addition to flow visualization, the reattachment length has been measured by LDV, and the results are depicted in Fig. 3 where L_r is the axial distance between the axial inlet port and the reattachment point. It can be seen that the reattachment length decreases nonlinearly with MR.

Based on the preceding description, the flow patterns in the present model can be characterized by the dome recirculation zone, axial jet zone, side jet zone, jet impingement zone, separation bubble, nozzle-like zone, developing zone, and fully developed zone, as summarized in Fig. 4.

Baseline Case: *MR* = 0.27

The momentum ratio of 0.27 of the axial- to side-inlet flow was selected as the baseline case because at this value of MR the flowfield in the chamber satisfies the conditions 1) good axial jet penetration and 2) strong axial/side jet mixing, which are two crucial factors to achieve high-combustion efficiency.[6,9] Figure 5 shows power spectral density functions of the velocity and wall pressure fluctuations measured at several locations inside the chamber for $MR = 0.27$. The most distinct peak at $f = 365$ Hz exists in the whole chamber and is identified as the fundamental frequency. For the longitudinal velocity spectra U, the energy level of this peak increases from 10^{-2} at $X^* = -0.27$ to 10^{-1} at $X^* = 0.27$ and 1.5 and then decreases to 10^{-2} at $X^* = 7.0$. For the transverse velocity spectra V, the energy levels of this peak at $X^* = -0.27$, 0.27, and 7.0 were about the order of 5×10^{-2} except on the order of 5×10^{-1} at $X^* = 1.5$. The abrupt one-order increase in the fluctuation energy of the transverse velocity at $X^* = 1.5$ is noted and may be due to the flapping motion of the separation layers located immediately downstream of the side-inlet ports.[11] The wall pressure spectra at $X^* = 1.5$ and 7.0 are also shown in Figs. 5c and 5d. The dominant frequencies of wall pressure fluctuations at $X^* = 1.5$ coincide with those of velocity spectra indicating the good correlation between the velocity and pressure. At the farther downstream location $X^* = 7.0$, the pressure spectral peaks smear because of the dissipation and the scattering of the wave energy associated with the downstream propagation of pressure waves.

The streamwise variation of the energy level of pressure fluctuation at the fundamental frequency ($f = 365$ Hz) is depicted in Fig. 6. This figure shows that the highest energy level occurs at $X^* = 1.3$ (or $L_r/H = 1.8$) which approximately coincides with the reattachment point (Fig. 3). This observation provides support in determining the distance from the axial-inlet exit to the reattachment point as the feedback length [$L \equiv \sqrt{(L_r^2 + (0.5H)^2)}$] which will be used in the feedback model shortly. As can be seen from Fig. 5, another distinct peak at $f = 730$ Hz is also detectable for $X^* = 0$ (not shown) to 0.27 and for $X^* = -0.27$–1.5 for the axial and transverse velocity spectra, respectively. The frequency $f = 730$ Hz of the second distinct peak is exactly double the fundamental frequency $f = 365$ Hz and is identified as the first harmonic frequency. To further examine the signals of velocity fluctuations, the time history of the axial and transverse velocities sampled at $(X^*, Y^*) = (0.27, 0.33)$ is analyzed. The axial velocity fluctuations are found to present the form of a slightly distorted sinusoidal wave with a time scale of 2.7 ms (or a frequency of 365 Hz), indicating the resonant frequency.[14] The time history of the transverse velocity, however, embodies more small zigzag fluctuations because of the contribution of the stronger second harmonic frequency (730 Hz).

Effects of *MR*

The momentum ratio of the axial- to side-inlet flow is an important factor affecting the flowfield structure.[6,9] Therefore, the spectral characteristics of the velocity and wall pressure for various MR

values were also investigated. The momentum ratio is defined as $MR = W_f U_a^2/(W_a U_s^2)$ and varied under a constant combustor Reynolds number of 4.56×10^4. Figures 7a–7f show the spectra of U- and V-component fluctuations at $(X^*, Y^*) = (0.27, 0.33)$ (about the center of impingement region) for MR ranging from 0.0094 to 1.28. A distinct peak at the fundamental frequency is detected, and the fundamental frequency increases with increasing MR, but for $MR = 1.28$ (Fig. 7g) no distinct peak is exhibited. The spectra of wall pressure fluctuations at $X^* = 1.5$, 2.8, and 7.0 under various MR values are shown in Fig. 8. The values of dominant frequencies of each case are coincident with those in corresponding velocity spectra. At $X^* = 1.5$ the energy level of the most distinct peak is high, and the second and/or third distinct peaks are also observed in the pressure spectra. As X^* increases to 2.8, the energy levels of these distinct peaks decrease because of the loss of the degree of coherence in the flow structure. At the farther downstream location $X^* = 7.0$, the peaks decay and divide into several small peaks in the low-frequency range.

Figure 9a depicts the variation of the fundamental frequency corresponding to the most distinct peak (f_d, solid diamond) in the spectral profiles with MR. It is seen that an approximately linear dependence can be fitted. The fitted line indicated as the solid line in the figure is

$$f_d = 608MR + 224\,\text{Hz} \tag{1}$$

If the data are presented in terms of the Strouhal number ($S = fW_f/U_a$) vs Reynolds number ($Re = W_f U_a/\nu$), as shown in Fig. 9b, the Strouhal number is nearly constant with a value of 0.013 in the range from $MR = 0.0094$–0.94. It should be pointed out that if one substitutes Eq. (1) into the definition of Strouhal number, one obtains the expression $S = 608W_f U_a/(2W_f U_s^2) + 224/U_a$ in which the first term increases and the second term decreases with Reynolds number so the value of Strouhal number remains approximately constant. Also, it is worth noting that a similar observation can be found in the jet-hole configuration investigated

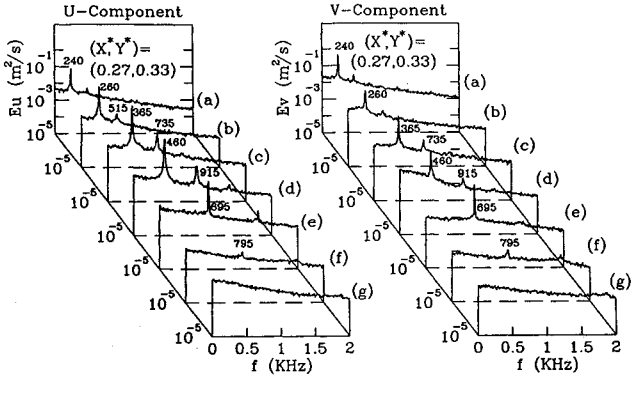

Fig. 7 Velocity spectra of U- and V-component fluctuations at $(X^*, Y^*) = (0.27, 0.33)$ for MR: a) = 0.0094, b) = 0.067, c) = 0.27, d) = 0.42, e) = 0.71, f) = 0.94, and g) = 1.28.

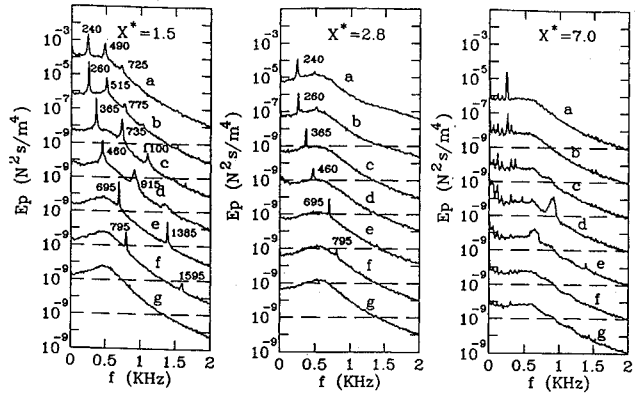

Fig. 8 Wall pressure spectra at X^* = 1.5, 2.8, and 7.0 for MR: a) = 0.0094, b) = 0.067, c) = 0.27, d) = 0.42, e) = 0.71, f) = 0.94, and g) = 1.28.

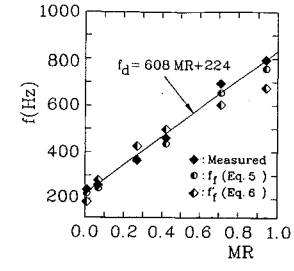

Fig. 9a Variation of the regression fitted feedback frequency, solid line; measured fundamental frequency, solid diamond; f_f, half solid circle; and f'_f, half solid diamond with MR.

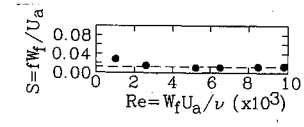

Fig. 9b Variation of Strouhal number with axial Reynolds number.

by Chanaud and Powell.[15] In their results the Strouhal number is almost constant for a certain Reynolds number range[15] and portrays hysteretic jumps between different ranges of Reynolds number. However, the hysteresis phenomenon is not observed in the present flowfield.

Generation of the Resonant Frequencies

For the case of the impingement flow oscillations, the main influential factors are the disturbance feedback mechanism, acoustic characteristics of boundary geometry, and resonance effects. As the fundamental frequencies of a flow match up with the oscillation mode of the boundary geometry, the large amplified oscillations may be triggered. The augment of oscillations associated with the boundary geometry can also be found by comparing the spectra of streamwise velocity fluctuations of the backward-facing step flow (without impingement edge) with flow over a cavity (with impingement edge).[1] In the present study, the dominant oscillation frequencies are observed in the MR range of 0.0094–0.71; however, in the cases of $MR = 0.94$ and 1.28, only weak peaks or no obvious peaks are detected. This observation will be discussed in the following.

First, a convective resonance model is considered. The model is based on the feedback mechanism; the pressure waves generated by the interaction between the jet coherent structures and walls in the impingement region propagate upstream and force the shear layers near the jet exit. The feedback frequencies f_f are predicted by the feedback equation[5,16]

$$N/f_f = L(1/U_c + 1/a_0) \tag{2}$$

where N is an integer number and taken as the value of unity for the fundamental frequency. U_c is the convective velocity and has been reported to be approximately 0.63 U_j (jet exit velocity) in a single-jet case. The feedback distance L has been taken as the distance from the nozzle lip to the flat plate for the case of the jet-plate impingement and is specified as the length from the axial jet exit to the reattachment point (Fig. 3) for the present case since the largest energy level of the fluctuating pressure, caused by the flapping motion of the shear layers and the collision between the shedding vortices and combustor walls, occurs at reattachment point (Fig. 6). Now the last quantity to be determined is the convective velocity U_c in the present flowfield as discussed in the following.

For the convective resonance model, the cross-correlation $R_{ij}(\tau)$ of the fluctuating pressures at two locations, x_i and x_j, would show four peaks with the following time delays according to different propagation routes[14]:

$$\begin{aligned} \tau_1 &= (x_j - x_i)/Uc, \qquad \tau_2 = -(x_j - x_i)/a_0 \\ \tau_3 &= -[(L - x_j)/U_c + (L - x_i)/a_0] \\ \tau_4 &= [(L - x_i)/U_c + (L - x_j)/a_0] \end{aligned} \tag{3}$$

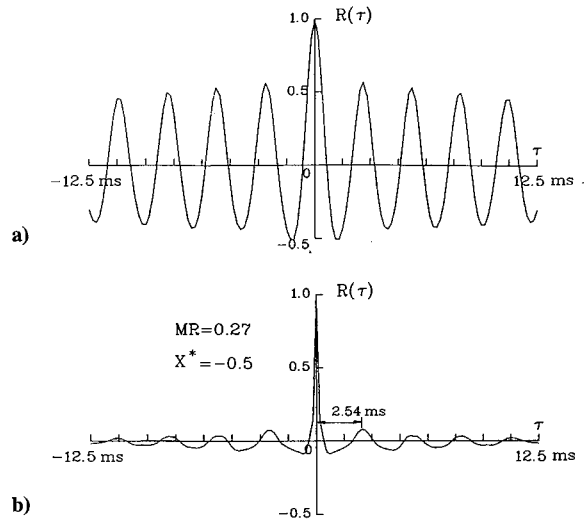

Fig. 10 Autocorrelation functions, at $X^* = 1.28$ for $MR = 0.27$: a) before prewhitening and b) after prewhitening.

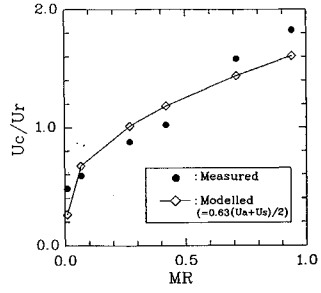

Fig. 11 Measured and modeled convective velocity for various values of MR.

where x_j and x_i are distance starting from the jet exit. If $x_j = x_i = 0$, i.e., for the case of the autocorrelation function sampled at the jet exit, the last equation could be rewritten as

$$\tau_1 = \tau_2 = 0$$
$$-\tau_3 = \tau_4 = L(1/U_c + 1/a_0) \tag{4}$$

Thus, U_c can be determined from this equation, i.e., $U_c = (\tau_4/L - 1/a_0)^{-1}$. Therefore, the feedback frequency f_f is given by

$$f_f = \frac{1}{L}\left(\frac{1}{U_c} + \frac{1}{a_0}\right)^{-1} \tag{5}$$

Because the spectra are dominated by the resonant frequency peak in the present study and the correlation functions would show a sinusoidal behavior with less distinguishable optimum peak, the prewhitening technique is used to analyze small random signals embedded in a strong pure tone. Figure 10 shows the autocorrelation functions at the jet exit ($X^* = -0.5$) for $MR = 0.27$ in which Fig. 10a is before prewhitening and Fig. 10b after prewhitening. A value of 2.54 ms is obtained for τ_4 which corresponding to $U_c = 22.3$ (m/s). The U_c for other values of MR are plotted in Fig. 11, and the feedback frequencies f_f calculated are shown in Fig. 9a (half-solid circle). With increasing MR, therefore, the feedback length (or reattachment length) decreases (Fig. 3) and the convective velocity increases (Fig. 11) such that the first fundamental feedback frequency increases (Eq. (5) and Fig. 9a).

Based on the idea of the mutual impingement and mixing of these flow streams, U_c may be modeled as the average velocity of the axial and the side flow velocities [that is, $U_c = 0.63(U_a + U_s)/2$], i.e.,

$$f_f' = \frac{1}{L}\left(\frac{1}{0.63(U_a + U_s)/2} + \frac{1}{a_0}\right)^{-1} \tag{6}$$

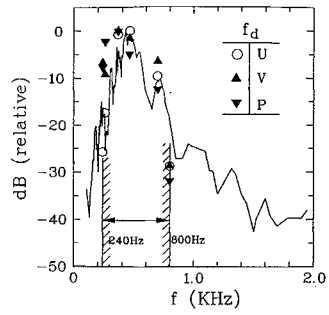

Fig. 12 Acoustic resonance curve of the chamber cavity and amplitude of f_d at $(X^*, Y^*) = (0.27, 0.33)$ for U and V at $X^* = 1.5$ for wall pressure under various MR values.

The predicted feedback frequencies f_f' at various MR are plotted in Fig. 9a (half-solid diamond) for comparison with f_d and f_f. The good agreement between the measured f_d and the predicted f_f and f_f' suggests that the mechanism of the flow induced oscillation in the present combustor chamber is well described by the feedback mechanism and U_c is well modeled by $U_c = 0.63(U_a + U_s)/2$.

The resonance effects are further examined in terms of the acoustic resonance curve of the chamber cavity to relate the coupling between the feedback frequency f_d and the acoustic cavity resonance response. The measured acoustic resonance curve of the chamber cavity is shown in Fig. 12. From this figure, it can be seen that the chamber cavity displays high gains (dB ≥ -20) in the range from 240 to 800 Hz with a peak at 420 Hz. As MR increases from 0.0094 to 0.27, f_d varies from 240 to 365 Hz according to Fig. 9, and there is an increase from -20 to -4 dB in Fig. 12, that is, coinciding with the high gain interval of the resonance curve. Consequently, the coupling between f_d and cavity resonance response is strengthened, and the amplitude of measured resonance frequency f_d (symbols in Fig. 12) is amplified in the corresponding frequency range. Similarly, as MR continues to increase from 0.42 to 0.94 and f_d correspondingly varies from 460 to 795 Hz, the amplitude of f_d decreases because the gain of the resonance curve declines from -2 to -20 dB and, in turn, the coupling is weakened. Eventually, as MR reaches 1.28 and the corresponding f_d would be 1 kHz, the coupling is too weak to sustain the oscillation at and beyond this frequency. Therefore, there is no peak frequency observed as $MR \geq 1.28$. Now, it is clear that the generation of the measured spectral peaks f_d results from the coupling between the feedback frequency f_f and the acoustic cavity resonance response.

Concluding Remarks

The following conclusions can be drawn from the present study.

1) The investigated flow patterns can be characterized by dome recirculation zone, axial jet zone, side jet zone, jet impingement zone, separation bubble, nozzle-like zone, developing zone, and fully developed zone.

2) It is found that the most dominant frequencies exist in the baseline case ($MR = 0.27$), which implies the presence of the well-organized coherent structures in the flowfield.

3) The dominant frequencies are found to increase with increasing MR for the investigatedMR range; however, the distinct spectral peaks disappear as $MR \geq 1.28$. A nearly linear correlation, $f_d = 608MR + 224$ (Hz), is found between the first fundamental frequency and MR; the Strouhal number is approximately constant for $10^3 < Re < 10^4$.

4) For the present ducted flow with multiple inlets, the observed flow induced oscillations are found to be well interpreted by the feedback mechanism model with appropriately proposed feedback distance (L, from axial jet exit to reattachment point) and measured convective speed of the coherent shedding vortices from the autocorrelation functions. The convective velocity could also be well modeled by $0.63(U_a + U_s)/2$. Moreover, the resonant phenomenon is triggered by the coupling between the feedback frequency and the acoustic resonance response of chamber.

Acknowledgment

Support for this work was provided by the National Science Council of the Republic of China under Contract NSC82-0424-E007-034.

References

[1]Rockwell, D., and Naudascher, E., "Self-Sustained Oscillations of Impinging Free Shear Layers," *Annual Review of Fluid Mechanics*, Vol. 11, 1979, pp. 67–94.

[2]Rockwell, D., "Oscillations of Impinging Shear Layers," *AIAA Journal*, Vol. 21, No. 5, 1983, pp. 645–664.

[3]Dunlap, R., and Brown, R. S., "Exploratory Experiments on Acoustic Oscillations Driven by Periodic Vortex Shedding," *AIAA Journal*, Vol. 19, No. 3, 1981, pp. 408, 409.

[4]Clark, W. H., "Experimental Investigation of Pressure Oscillations in a Side Dump Ramjet Combustor," *Journal of Spacecraft and Rockets*, Vol. 19, No. 1, 1982, pp. 47–53.

[5]Byrne, R. W., "Longitudinal Pressure Oscillations in Ramjet Combustors," AIAA Paper 83-2018, June 1983.

[6]Schadow, K. C., and Chieze, D. J., "Water Tunnel and Windowed Combustion as Tools for Ducted Rocket Development," *Proceedings of the 18th JANNAF Propulsion Meeting*, CPIA-PUB-340, Vol. 2, 1981, pp. 101–115.

[7]Chuang, C. L., Cherng, D. L., Hsieh, W. H., Settles, G. S., and Kuo, K. K., "Study of Flowfield Structure in a Simulated Solid-Propellant Ducted Rocket Motor," AIAA Paper 89-0011, Jan. 1989.

[8]Hseih, W. H., Chuang, C. L., Yang, A. S., Cherng, D. L., Yang, V., and Kuo, K. K., "Measurement of Flowfield in a Simulated Solid-propellant Ducted Rocket Combustor Using Laser Doppler Velocimetry," AIAA Paper 89-2789, July 1989.

[9]Liou, T. M., and Wu, Y. Y., "Turbulent Flows in a Model SDR Combustor," *Journal of Fluids Engineering*, Vol. 115, Sept. 1993, pp. 468–473.

[10]Schadow, K. C., Wilson, K. J., and Gutmark, E., "Characterization of Large-Scale Structures in a Forced Ducted Flow with Dump," *AIAA Journal*, Vol. 25, No. 9, 1987, pp. 1164–1170.

[11]Liou, T. M., Wu, S. M., and Hwang, Y. H., "Experimental and Theoretical Investigation of Turbulence Flow in a Side-Inlet Rectangular Combustor," *Journal of Propulsion and Power*, Vol. 6, No. 2, 1990, pp. 131–138.

[12]Tropea, C., "Turbulence-Induced Spectral Bias in Laser Anemometry," *AIAA Journal*, Vol. 25, No. 2, 1987, pp. 306–309.

[13]Adrian, R. J., and Yao, C. S., "Power Spectra of Fluid Velocities Measured by Laser Doppler Velocimetry," *Experiments in Fluids*, Vol. 5, 1987, pp. 17–28.

[14]Ho, C. M., and Nosseir, N. S., "Dynamics of an Impingement Jet. Part 1. The Feedback Phenomenon," *Journal of Fluid Mechanics*, Vol. 105, 1981, pp. 119–142.

[15]Chanaud, R. D., and Powell, A., "Some Experiments concerning the Hole and Ring Tone," *Journal of the Acoustical Society of America*, Vol. 37, No. 5, 1965, pp. 902–911.

[16]Nosseir, N. S., Peled, U., and Hildevrand, G., "Pressure Field Generated by Jet-on-Jet Impingement," *AIAA Journal*, Vol. 25, No. 10, 1987, pp. 1312–1317.